The impact of wood-derived gasification gases on Ni-CGO anodes in intermediate temperature solid oxide fuel cells

Sylvia Baron, Nigel Brandon*, Alan Atkinson, Brian Steele, Robert Rudkin

Centre for Ion Conducting Membranes, Imperial College London, South Kensington, SW7 2AZ London, UK

Abstract

The impact of gases arising from the gasification of wood chips on the performance of an intermediate temperature solid oxide fuel cell (IT-SOFC) has been assessed. The anode material was a 60:40 wt.% Ni:CGO-10 ($Ce_{0.9}Gd_{0.1}O_{1.95}$) cermet, which was tested in various gas atmospheres from diluted hydrogen to emulated gasification mixtures containing H_2, N_2, CO, CH_4 and CO_2. It was found that CO decreased the performance of the cell when compared to H_2. The presence of 10% CO_2 in the fuel did not significantly affect cell performance, whilst operation with 5 and 10% CH_4 resulted in poor power output due to carbon deposition. The current–voltage characteristics of the cell in hydrogen compared well with theoretical I/V predictions. The latter enable leakage currents, arising from the partial reduction of the CGO electrolyte on the anode side, to be quantified.
© 2003 Elsevier B.V. All rights reserved.

Keywords: SOFC; IT-SOFC; Anode; Ni-CGO; Biofuel; Gasification

1. Introduction

The importance of replacing fossil fuels with sustainable and renewable energy sources in order to achieve a reduction in greenhouse gas emissions is of great concern. Small-scale gasification has been identified as a significant source of gaseous biofuels for heat and electricity generation. Wood chip gasification results in gas compositions of 40–50% N_2 + 22–27% CO + 15% H_2 + 10–15% CO_2 + 2–3% CH_4 [1]. The gases produced are used in engines and turbines with fairly low efficiencies and generate significant amounts of regulated pollutants (NO_x, SO_x, and particulates).

Replacement of these conventional heat engines with fuel cells would allow a more efficient use of biofuels but, more significantly, would reduce NO_x to insignificant levels and increase CO_2 benefits.

However, the impact of using a biofuel within a fuel cell is not well established. The application of biofuel in a fuel cell has been discussed by several authors [2–15] but in nearly all cases the work has been based on paper studies of system performance, and has largely, though not exclusively, concentrated on the Molten Carbonate Fuel Cell (MCFC). Exceptions include the work of Kiros et al. [2], who studied

a biomass fuelled alkaline fuel cell, Alderucci et al. [9] who carried out a thermodynamic study of an integrated biomass catalytic gasifier-solid oxide fuel cell (SOFC) system, and Staniforth and Kendall [10] who used simulated biogas to power a small tubular SOFC.

Of all the fuel cell types, the SOFC is likely to possess a greater level of tolerance to contaminants as well as provide the opportunity for internal reforming of the biofuel. Intermediate temperature SOFCs (IT-SOFCs) have been chosen as the basis for this study. The advantages and issues of operating at this temperature have been discussed by Steele et al. [16–18] and Huijsmans et al. [19].

Zhu et al. [20] experimentally studied the impact of gasification gases on an IT-SOFC, but the cell electrodes used were based on salt-oxide composite (SOC) with Ni-based oxides and fluorides. However, the SOC catalyst electrodes showed a high sensitivity to nitrogen concentration, resulting in a significant reduction of the cell open circuit voltage (OCV) when nitrogen was present in the fuel gas stream. Therefore, this anode material would not be feasible with the gasification gases studied in this work, which contain up to 50% N_2. Zhu recommended the use of ceria for the electrodes.

The aim of this study is to consider the impact of one renewable fuel source, namely that arising from the gasification of wood chips, on IT-SOFC performance, and specifically on anode behaviour. The materials chosen were

* Corresponding author. Tel.: +44-7594-5704; fax: +44-7594-5604.
E-mail address: n.brandon@imperial.ac.uk (N. Brandon).

$Ce_{0.9}Gd_{0.1}O_{1.95}$ (CGO-10) electrolytes with Ni-CGO cermet anodes. Although yttria-stabilised zirconia (YSZ) has shown very satisfactory results when used with nickel as an anode for SOFCs, at intermediate temperatures doped cerium oxides exhibit higher ionic conductivity than YSZ. Furthermore, the mixed conductivity of CGO should increase the reaction surface area by facilitating electron and oxygen ion transport in the anode [16,21,22].

2. Experimental

2.1. Ni-CGO anode

A Ni-CGO cermet was prepared using 40 wt.% CGO-10 (Rhodia) and 60 eq.wt.% Ni in the form of green NiO (Alpha Aesar) mixed with additives such as binder, dispersant, plasticiser and solvent. The anode material was characterised after reduction by 4-point dc lateral conductivity measurements in 10% H_2/N_2 + 2.3% H_2O, which gave a lateral conductivity of 942 S cm^{-1} at 682 °C on an 11 μm thick reduced anode.

Previous work [23,24] on 2-electrode impedance spectroscopy measurements on anode half cells in reducing conditions has shown that the data from that technique is affected by the reduction of CGO in the electrolyte pellet support, resulting in apparent large capacitance values at low frequencies. As a result, this work focused on fabricating and testing anode structures in a full fuel cell configuration.

2.2. Cell preparation

An electrolyte supported cell was prepared in order to assess anode performance under load in various gas compositions. The cell consisted of a dense CGO-10 electrolyte pellet (550 μm thick), an LSCF-CGO (70 wt.% $La_{0.6}Sr_{0.4}Co_{0.2}Fe_{0.8}O_{3-\delta}$–30 wt.% $Ce_{0.8}Gd_{0.2}O_{1.9-x}$) cathode (15 μm thick) [25] and a Ni-CGO anode (13 μm thick). The CGO-10 electrolyte powder (Praxair) was pressed in a 16 mm diameter die with 1 t load and fired at 1450 °C for 2 h. The pellet diameter after firing was 11.6 mm. An anode layer was doctor bladed on one side of the electrolyte pellet using the Ni-CGO material described previously. Only the central area of the electrolyte, 8 mm in diameter, was covered with the anode material, leaving a small external ring for the cell glass sealing. The active cell area was thus defined by the anode to be approximately 0.5 cm^2. The combined structure was then sintered at 1300 °C for 2 h in air. A platinum mesh was used as current collector and bonded to the anode layer by covering the mesh with some Ni-CGO slurry and pressing it onto the anode, followed by a second identical sintering step. The anode layer was therefore slightly thicker than 13 μm.

The cathode layer was sprayed onto the whole surface of the other side of the electrolyte pellet using a LSCF-CGO slurry and sintered at 850 °C for 2 h. Subsequently, some slurry was painted onto a second platinum current collector mesh, pressed onto the cathode and sintered at 850 °C for 2 h.

Glass sealant (DuPont Encapsulant) was painted onto the non-coated ring on the anode side and placed on a zirconia tube with the anode side facing the inside of the tube. A platinum wire was welded onto each platinum mesh for electrical contacts and a thermocouple was placed next to the anode side. The assembly was placed in a horizontal tube furnace and fired in air at 850 °C for 0.5 h to seal the cell on the zirconia tube. The cathode side was left in ambient air, whereas fuel mixtures were fed onto the anode through a small ceramic tube, 2 mm away from the anode.

2.3. Cell performance testing

The cell was tested in moist hydrogen/nitrogen mixtures and in various emulated gasification mixtures. Experiments were performed at atmospheric pressure at 650 °C.

Steady state current–voltage characteristics of the cell were obtained using a Solartron 1287 potentiostat in galvanostatic mode. Complex impedance plots were acquired using a Solartron 1260 Impedance Analyser.

Fuel mixtures were controlled by mass flow meters (Bronkhorst). The total gas flow rate was maintained between 30 and 40 ml min^{-1}. The gas stream was humidified by passing the outlet of the gas line through a water bubbler. The bubbler was placed in a water bath, allowing the steam content to be varied by controlling the water temperature.

2.4. Microstructural characterisation

After the performance tests, the cell was cooled down to room temperature under the testing environment, cross-sectioned and polished down to a 1 μm diamond finish. The microstructure of the electrode and electrolyte layers was characterised using an analytical Scanning Electron Microscope (SEM). In order to obtain a micrograph of the anode material with no carbon deposition, a separate anode sample was prepared in the same condition as the cell, reduced in 10% H_2/N_2 and fractured to be analysed by SEM.

3. Results and discussion

3.1. Microstructure of the cell

Fig. 1 reveals the anode fracture surface of the separate anode sample. Furthermore, Fig. 2 shows the cathode–electrolyte interface. SEM examination of the cell cross-section revealed a satisfactory electrolyte of approximately 94% of theoretical density, which did not exhibit interconnected porosity.

The cathode layer contained angular elongated grains, which originate from a coarse particle size fraction in the CGO electrolyte.
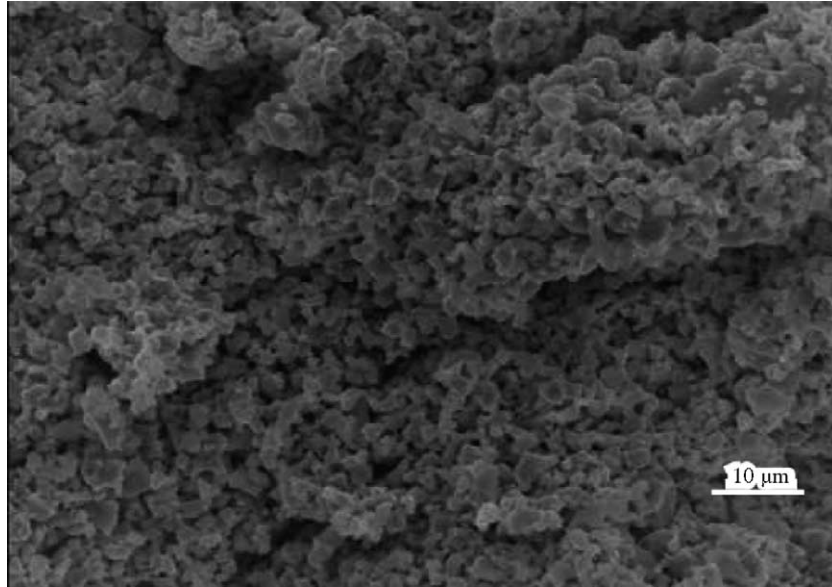
Fig. 1. SEM micrograph revealing the fracture surface of the anode layer after reduction in 10% H_2/N_2 at 700 °C for 0.5 h.

3.2. Cell operation in moist hydrogen

The cell was first fed with 10% H_2/N_2 + 2.3% H_2O at 650 °C in order to reduce NiO to Ni in the anode. A current density of 40 mA cm^{-2} was then applied to the cell for 2 h until a steady cell voltage was obtained. The OCV was 0.88 V.

Subsequently, the hydrogen concentration was increased to 20% and then to 50%, which resulted in an increase of the OCV to 0.89 and 0.93 V, respectively. Fig. 3 shows the *I/V* curve in 10, 20 and 50% H_2/N_2 + 2.3% H_2O. As expected, the cell power density increased with increasing H_2 concentration. Although factors such as the thick electrolyte, dilute fuel at the anode and stagnant air at the cathode side are
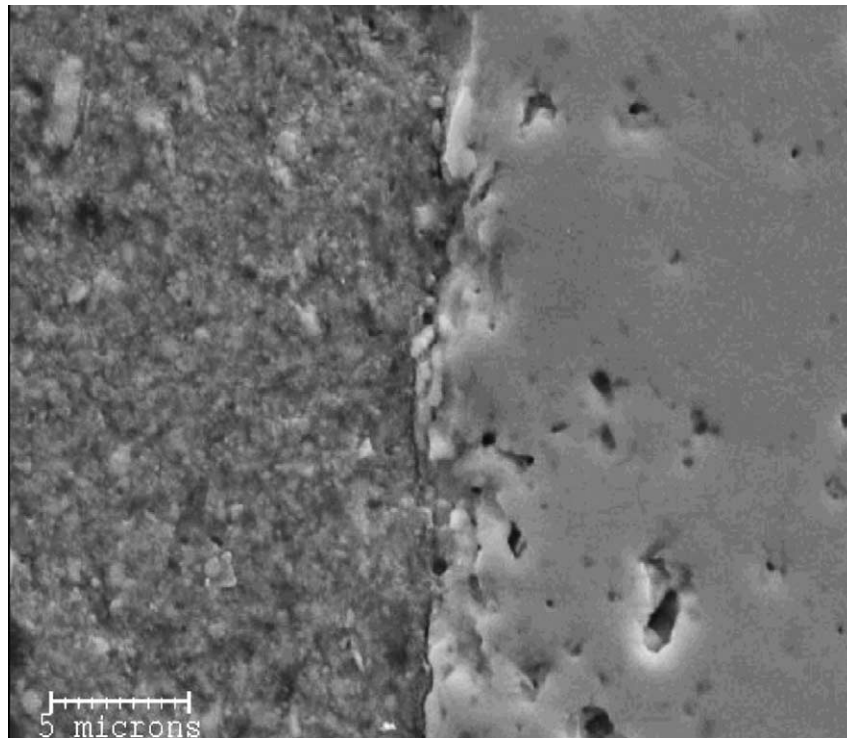

Fig. 2. SEM cross-sectional micrograph of the cathode–electrolyte interface taken after the cell test. Image analyses indicated that the LSCF-CGO cathode has a relative density of 14% and the CGO electrolyte 94% of theoretical density.
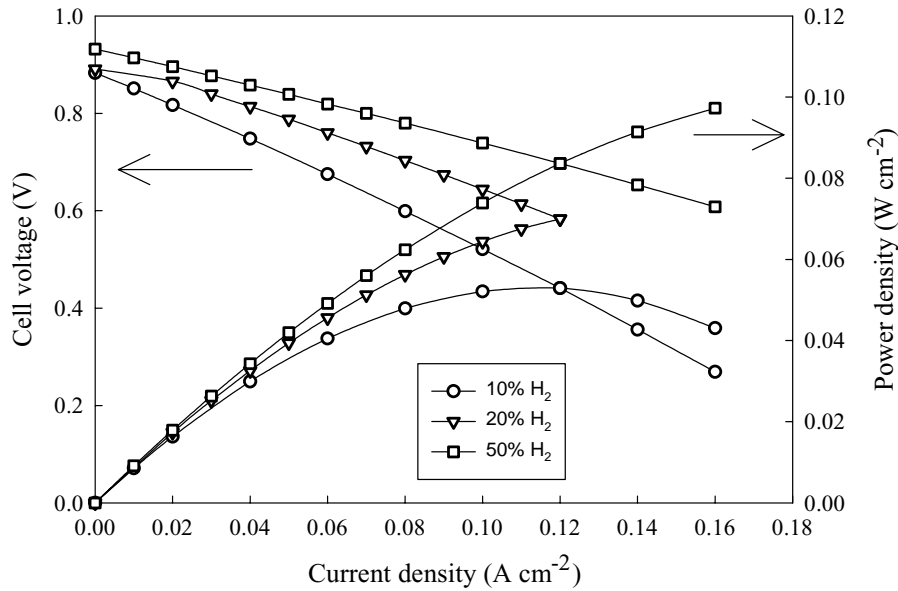
Fig. 3. Current–voltage results for the cell operating at 650 °C under 10, 20 and 50% H_2/N_2 + 2.3% H_2O.

expected to considerably reduce the cell performance, the current and voltage results were sufficiently encouraging to warrant further testing in various fuel compositions.

In order to extract the anode overpotential from the cell results, the cathode and electrolyte potential drops had to be measured. The current–overpotential behaviour of the LSCF-CGO cathode was obtained from independent three electrode measurements on CGO electrolyte [26]. Electrolyte ionic losses were evaluated using the area specific resistance (ASR = $1.8\,\Omega\,cm^2$) of CGO-10 (Praxair) obtained experimentally in air at 650 °C from a 730 μm thick pellet.

The resulting electrolyte potential drop and cathode overpotential are shown in Fig. 4, from which the anode overpotential value can be extracted. At a current density of $0.1\,A\,cm^{-2}$, the anode overpotential was found to be 0.13 V, equivalent to an anode ASR of $1.3\,\Omega\,cm^2$. However, this analysis neglects the effect of the partial electronic conductivity of the electrolyte.

In order to check this effect, theoretical current–voltage characteristics were calculated for the cell using the model developed by Godickemeier and co-workers [27,28], modified by Steele [16] and discussed in [29]. The model accounts for the presence of partial short circuiting electronic
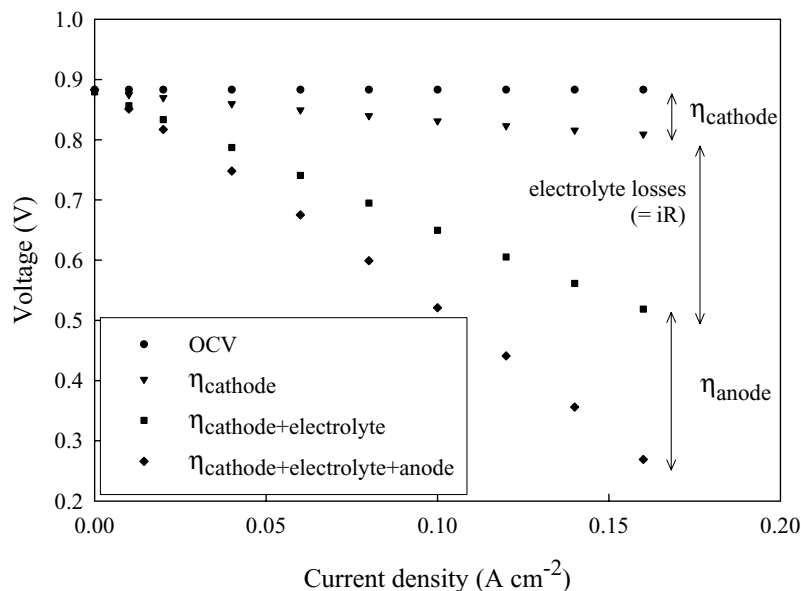

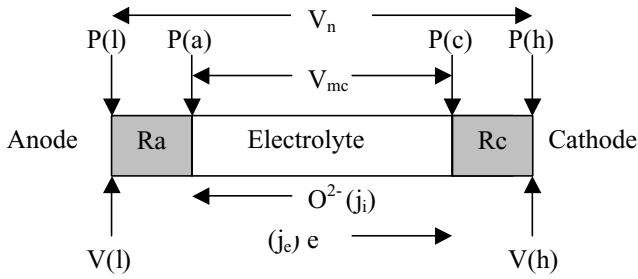Fig. 4. Cell cathode, electrolyte and anode overpotentials at 650 °C in 10% H_2/N_2 + 2.3% H_2O.

Fig. 5. Schematic diagram of a mixed electrolyte cell.

currents due to the electrolyte mixed conductivity, even under OCV conditions. This results in a decrease of the OCV, as well as changes in the pO_2 at both anode and cathode interfaces with the electrolyte.

Fig. 5 represents a schematic cross-section of the SOFC and illustrates the model. $P(l)$ and $P(h)$ are the anode and cathode oxygen partial pressures imposed by the external fuel and oxidant. The anode and cathode potentials, $V(l)$ and $V(h)$ at the low and high pO_2, respectively, can thus be determined together with V_n, the Nernst voltage. However, in order to account for the anode and cathode polarisation losses R_a and R_c, the actual oxygen partial pressure $P(a)$ and $P(c)$ at the electrolyte/anode and electrolyte/cathode interfaces were defined.

$$V_{mc} = V_{th} - j_i R_i \tag{1}$$

where

$$V_{th} = V_n - j_i(R_a + R_c) \tag{2}$$

Thus,

$$V_{mc} = V_n - j_i(R_i + R_a + R_c) \tag{3}$$

where j_i is the oxygen ion current passing through the electrolyte and R_i is the electrolyte ionic resistance. Under OCV conditions $j_e = j_i$ and the equation for j_e [4], the electronic leakage current, can thus be solved.

$$j_e = \frac{\sigma_i}{L} \left(\frac{P(-)}{\exp(-4RT/F(V_h + j_i R_c))} \right)^{1/4} (j_i R_i)$$
$$\times \frac{\exp(F/RT(V_n - j_i(R_i + R_a + R_c))) - 1}{1 - \exp(-F/RT j_i R_i)} \tag{4}$$

σ_i is the electrolyte ionic conductivity; L is the electrolyte thickness; $P(-)$ is the oxygen partial pressure at which $\sigma_e = \sigma_i$ with σ_e being the electrolyte electronic conductivity; R is the molar gas constant; F is the Faraday constant; and T is the temperature in Kelvin (K). The $P(-)$ value for CGO-10 calculated from Steele [16] was found to be 8.83×10^{-23} atm. However, Steele [16] also reported that the theoretical $P(-)$ value and the experimentally obtained $P(-)$ values often show some discrepancy. The $P(-)$ is specific to each CGO powder and therefore, for this work, a best fit value of 3.25×10^{-24} atm was used.

The model cell characteristics are plotted in Fig. 6 where they are compared with the experimental data for 50% H_2 reproduced from Fig. 3. The anode ohmic resistance used in the model was varied, and a value of $1.5\,\Omega\,cm^2$ gave a good fit to the experimental curve. This anode resistance is close to that extracted using overpotential data ($1.3\,\Omega\,cm^2$, see Fig. 4). The lower experimental OCV (0.93 V) than the Nernst potential (1.11 V) arises from the partial reduction of the CGO electrolyte at the anode side. The leakage current at open circuit was calculated to be $0.05\,A\,cm^{-2}$ under these conditions.
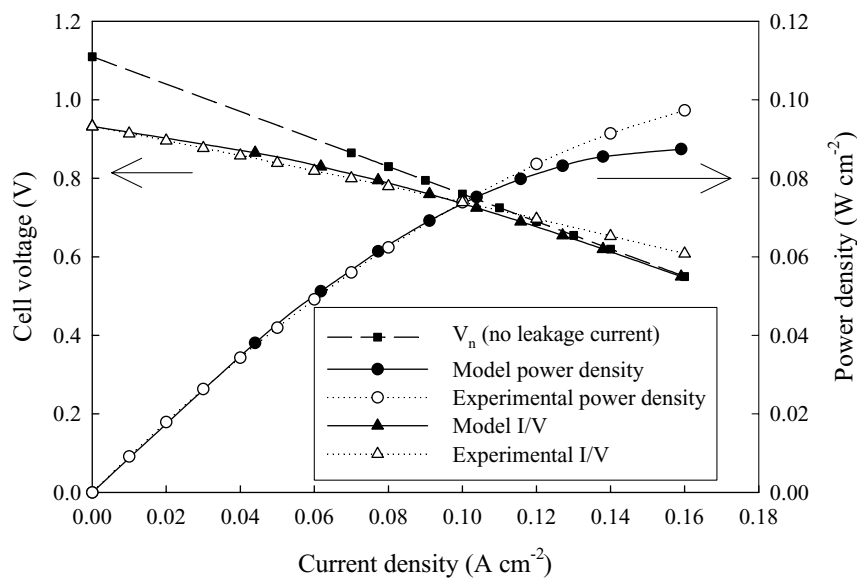

Fig. 6. Comparison of the experimental and modelled current–voltage characteristics of the cell at 650 °C with air as the oxidant and 50% $H_2/N_2 + 2.3\%$ H_2O as the fuel. Also shown is the Nernst voltage (V_n), in the absence of leakage current. Model parameter values: $L = 550\,\mu m$; $T = 923\,K$; $R_i = 1.8\,\Omega\,cm^2$; $R_a = 1.5\,\Omega\,cm^2$; $R_c = 0.2\,\Omega\,cm^2$; $pO_2(c) = 0.2\,bar$; $pO_2(a) = 1.14E{-}25\,bar$; $P(-) = 3.25E{-}24\,bar$.
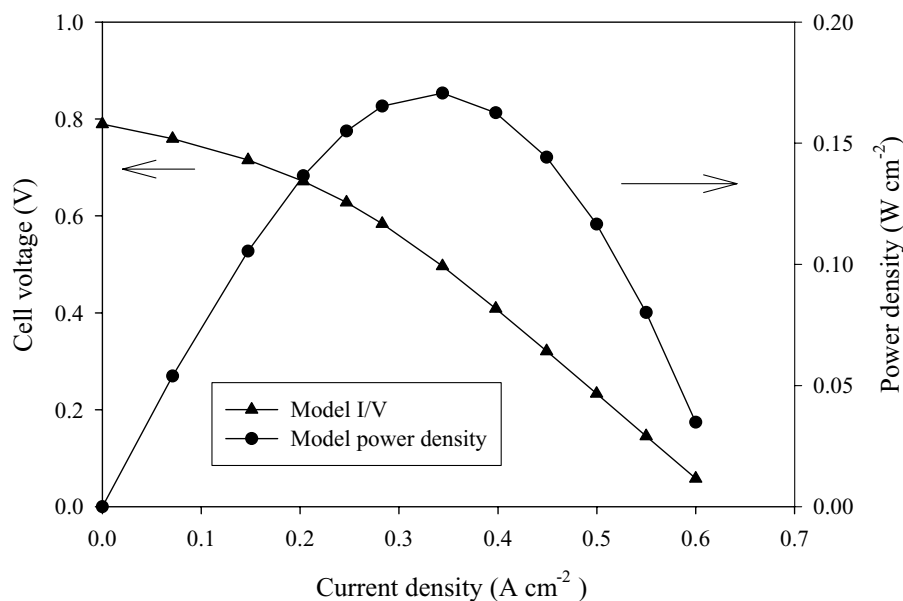
Fig. 7. Modelled current–voltage characteristics of the cell at 650 °C with air as the oxidant and 50% H_2/N_2 + 2.3% H_2O as the fuel. All parameter values are the same as for Fig. 5, except that $L = 20\,\mu m$; leading to $R_i = 0.053\,\Omega\,cm^2$.

The model was then used to predict the *I/V* characteristics of a cell with $20\,\mu m$ thick electrolyte instead of $550\,\mu m$. All other parameters were kept the same as for the tested $550\,\mu m$ cell. Fig. 7 shows that a maximum power output of $0.17\,W\,cm^{-2}$ could be achieved if the electrolyte thickness was reduced to $20\,\mu m$ (assuming a linear polarisation resistance of the electrodes).

Impedance spectroscopy was performed on the experimental cell under the same fuel conditions at a current density of $20\,mA\,cm^{-2}$. Results were corrected for the ohmic loss due to the thick electrolyte pellet at high frequencies, and normalised to electrode area. Fig. 8 shows the presence of two semi-circles on the Cole-Cole plots. The high frequency (HF) arc (frequencies > 100 Hz) was relatively independent of the hydrogen concentration, whereas the low frequency (LF) arc was strongly affected by the H_2 content. Effectively, the LF arc resistance exhibits an approximate $(pH_2)^{-1}$ dependency. This suggests that the LF feature might be dominated by mass transport limitations arising from transport in the gas phase within the anode. This is con-

sistent with independent measurements on the LSCF-CGO cathode, which suggest a negligible contribution of the order of $1\,m\Omega\,cm^2$ from gas transport limitations in air at 650 °C on the cathode. This influence of the anode gas phase diffusion at LF is also consistent with the anode's fine pore structure and highlights the need for optimisation of the anode pore structure to improve anode performance.

3.3. Cell operation in gasification gases

Fig. 9 presents the anode overpotential for various gas mixtures from moist 25% H_2 to a simulated biofuel composition. The anode overpotential was extracted from the cell *I/V* characteristics using the subtraction method described for moist hydrogen. The impact of CO and CO_2 are evident from the plot. CO does not poison the anode, as moist 25% H_2 + 25% CO shows a slightly higher power density than moist 25% H_2. However, moist CO alone gave a high anode overpotential. On the other hand, the addition of 10% CO_2 in a moist 15% H_2 + 25% CO resulted in only a very small
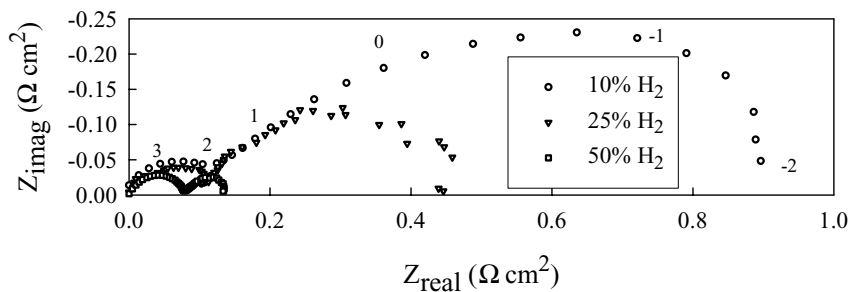

Fig. 8. Cole-Cole impedance plots at 650 °C at $20\,mA\,cm^{-2}$ in 10, 20 and 50% H_2/N_2 + 2.3% H_2O/air. Log scale frequencies are presented next to the 10% H_2 plot.
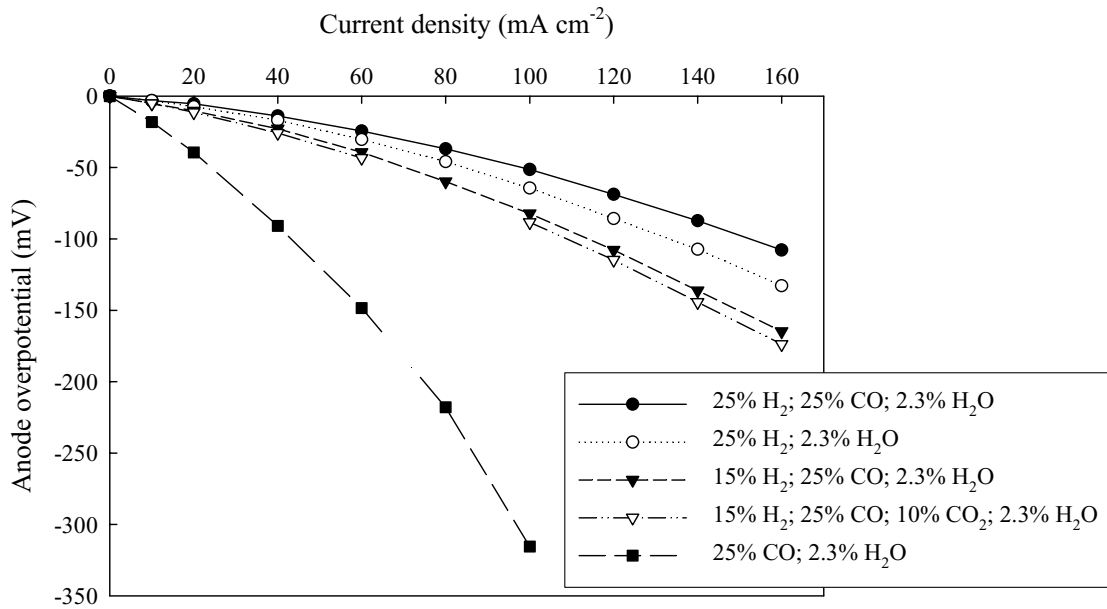
Fig. 9. Impact of various H_2, CO and CO_2 concentrations on the anode overpotential. $T = 650\,°C$. Diluent gas: N_2. Oxidant: air.

drop in performance. This indicates that CO_2 acts only as a diluent and that the slight drop in performance is due to the lower pH_2 at the fuel side arising from its replacement with CO_2.

These observations are also evident from the impedance plots presented in Fig. 10.

The HF semi-circle is the response associated with charge transfer process at both the anode and cathode. The increase in the HF arc diameter with changes in fuel composition is qualitatively proportional to the anode ASR increase, given

that the cathode ASR is expected to be constant and independent of the anode fuel content. The results are summarised in Table 1.

Table 1 shows that for 50% fuel, replacing 50% $H_2 + 2.3\%$ H_2O with a gasification mixture (15% H_2; 25% CO; 10% CO_2 and 2.3% H_2O) increases the electrode ASR (HF arc) by a factor of 2.2.

Moreover, Fig. 10 and Table 1 reveal the high dependence of the LF arc on the nature of the fuel. For example, when H_2 and CO are compared, the LF arc diameter for 25%
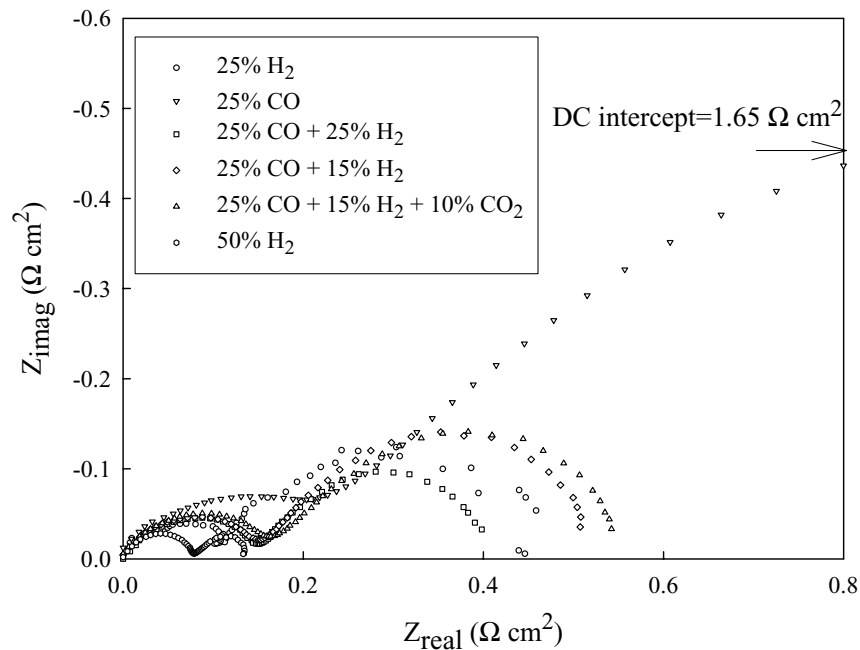

Fig. 10. Cole-Cole impedance plots at $T = 650\,°C$ at $20\,mA\,cm^{-2}$ in various fuel mixtures of N_2, H_2, CO and $CO_2 + 2.3\%$ H_2O/air.

Table 1
Effect of fuel composition on the relative anode ASR from the impedance plots of Fig. 10

Gas composition	HF ASR ($\Omega\,cm^2$)	HF relative ASR	LF ASR ($\Omega\,cm^2$)	LF relative ASR
50% H_2	0.08	1	0.05	1
25% H_2	0.15	1.9	0.35	7.0
25% H_2, 25% CO	0.16	2.0	0.26	5.2
15% H_2, 25% CO	0.17	2.1	0.38	7.6
15% H_2, 25% CO, 10% CO_2	0.18	2.2	0.40	8.0
25% CO	0.25	3.1	1.4	28.0

50% H_2 was taken as the reference (relative ASR set to 1). All gas mixtures are in N_2 + 2.3% H_2O.

H_2 is 0.35 $\Omega\,cm^2$, whereas it is four times larger for 25% CO (1.4 $\Omega\,cm^2$). It is believed that the LF arc is related to gas phase diffusion within the anode. Bulk binary diffusion coefficients were calculated [30] for CO and H_2 in N_2 using Eq. (5).

$$D_{AB} = \frac{0.0018583 T^{3/2}}{P(\sigma_{AB})^2 \Omega_{D,AB}} \sqrt{\frac{1}{M_A} + \frac{1}{M_B}} \tag{5}$$

where T is the temperature (K); P is the pressure (atm); D_{AB} is the binary diffusion coefficient (cm^2/s); M_X is the molecular weight for gas X (g mol^{-1}); k_B is the Boltzmann's constant; σ_{AB} is the Lennard–Jones "force constant" (Å); and $\Omega_{D,AB}$ is the collision integral related to $k_B T/\varepsilon_{AB}$, which can be found in [30].

At 650 °C and $P = 1$ atm, it was found that $D_{H_2/N_2} = 4.87 \times 10^{-4}\,m^2\,s^{-1}$ and $D_{CO/N_2} = 1.36 \times 10^{-4}\,m^2\,s^{-1}$, i.e. the binary diffusion coefficient of H_2/N_2 is 3.6 times faster than that for CO/N_2. This is consistent with the observed increase in the LF arc resistance. This supports the hypothesis that the LF response can be attributed to gas transport limitation in the anode, and highlights the need for a more porous anode material.

Finally, the steam content was increased to 10%, and 5% CH_4 was added to a 50% H_2/N_2 mixture so as to assess the impact of the presence of methane. The sequence of gas compositions and the corresponding cell terminal potential are listed in Table 2. It can be seen that the use of 10% CH_4 resulted in a significant drop in cell performance. This is illustrated in Fig. 11, which shows that the effect of CH_4 on

Table 2
Impact of CH_4 on the cell voltage

Time (min)	H_2 (%)	CH_4 (%)	H_2O (%)	V (V)
0	50	0	2.3	0.765
45	50	0	10	0.760
55	50	5	10	0.751
75	50	10	10	0.748
90	50	0	10	0.751

Time, gas composition and cell terminal potential under 20 mA cm^{-2} at 650 °C.

the cell impedance data at 650 °C. The total cell resistance, i.e. the distance on the Z_{real} axis between the high frequency and the low frequency intercept, increased as CH_4 was added to the gas mixture. The LF arc diameter increased most significantly with increasing CH_4 concentration. However, the resistance did not fully recover on removing the CH_4. This suggests that CH_4 has caused carbon deposition and partial blocking of the anode pores. Carbon deposition was evident from the examination of the cell after test.

4. Conclusion

Experimental current–voltage curves compared favourably with those predicted by a model of a CGO-based IT-SOFC. The model enables the open circuit cell leakage current to be predicted, which was 0.05 A cm^{-2} under the condition used (650 °C, 50% H_2/N_2 + 2.3% H_2O/air). Anode performance
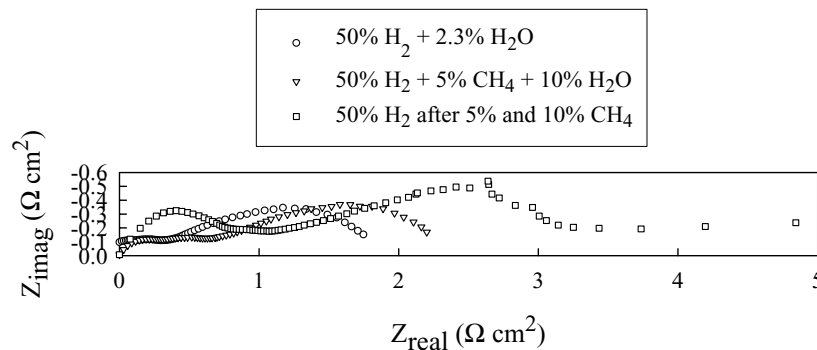

Fig. 11. Cole-Cole plots of the cell at $T = 650$ °C under 20 mA cm^{-2} before, during and 2 h after the introduction of 5 and 10% CH_4 to wet 50% H_2.

decreased when H_2 was replaced by CO in the fuel stream. In particular, gas transport in the anode was inhibited, reflecting the decreased diffusion coefficient of CO relative to H_2. Therefore, a more open anode microstructure is required for use with CO in order to suppress mass transport limitations. CO_2, at least at the levels present in wood derived gasification gases, did not affect anode performance. Addition of methane at a concentration of 10% decreased anode performance but further work is needed to clarify this behaviour. Future work will focus on developing anodes with improved microstructure, better able to operate on CO rich fuels, together with methane and sulphur tolerant materials.

Acknowledgements

References

[1] T.V. Ramachanda, N.V. Joshi, D.K. Subramanian, Renewable Sustainable Energy Rev. 4 (2000) 375–430.
[2] Y. Kiros, C. Myren, S. Schwartz, A. Sampathrajan, M. Ramanathan, Int. J. Hydrogen Energy 24 (6) (1999) 549–564.
[3] D. McIlveen-Wright, B.C. Williams, J.T. McMullan, Dev. Chem. Eng. Mineral Process. 7 (1/2) (1999) 85–114.
[4] D. McIlveen-Wright, D.J. Guiney, J. Power Sources 106 (2002) 93–101.
[5] K.V. Lobachyov, H.J. Richter, Energy Convers. Manage. 39 (16–18) (1998) 1931–1943.
[6] R.A. Knight, M. Onischak, F.S. Lau, Proc. Am. Power Conf. I (1998) 586–591.
[7] R.H. Borgwardt, Biomass Bioenergy 12 (5) (1997) 333–345.
[8] C.M. Kinoshita, S.Q. Turn, R.P. Overend, R.L. Bain, Proc. Am. Power Conf. 1 (1996) 727–732.
[9] A. Alderucci, P.L. Antonucci, G. Maggio, N. Giordano, V. Antonucci, Int. J. Hydrogen Energy 19 (4) (1994) 369–376.
[10] J. Staniforth, K. Kendall, J. Power Sources 71 (1998) 275–277.
[11] T. Kivisaari, P. Bjornbom, C. Sylwan, J. Power Sources 104 (2002) 115–124.
[12] B.J.P. Buhre, J. Andries, EURO Conference on New and Renewable Technologies for Sustainable Development, Kluwer Academic Publishers, Madeira, 2000.
[13] J. Smeenk, G. Steinfeld, R.C. Brown, E. Simpkins, M.R. Dawson, Proceedings of Third Biomass Conference of the Americas, Making a Business from Biomass, vol. 2, Montreal, Canada, 1997.
[14] R.J. Spiegel, J.L. Preston, J. Power Sources 86 (2000) 283–288.
[15] U. Langnickel, First European fuel cell application using digester gas, Fuel Cells Bull. 22 (2000) 10–12.
[16] B.C.H. Steele, Solid State Ionics 129 (2000) 95–110.
[17] B.C.H. Steele, A. Heinzel, Nature 414 (2001) 345–352.
[18] K. Choy, W. Bai, S. Charojrochkul, B.C.H. Steele, J. Power Sources 71 (1998) 361–369.
[19] J.P.P. Huijsmans, F.P.F. VanBerkel, G.M. Christie, J. Power Sources 71 (1998) 107–110.
[20] B. Zhu, X.Y. Bai, G.X. Chen, W.M. Yi, M. Bursell, Int. J. Energy Res. 26 (2002) 57–66.
[21] S. Wang, T. Kobayashi, M. Dokiya, T. Hashimoto, J. Electrochem. Soc. 10 (2000) 3606–3609.
[22] O.A. Marina, C. Bagger, S. Primdahl, M. Mogensen, Solid State Ionics 123 (1999) 199–208.
[23] S. Baron, N.P. Brandon, A. Atkinson, B.C.H. Steele, J. Electrochem. Soc., submitted for publication.
[24] S. Baron, N. Brandon, A. Atkinson, B.C.H. Steele, A. Bauen, D. Hart, in: J. Huijsmans (Ed.), Proceedings of Fifth European Solid Oxide Fuel Cell Forum, vol. 1, Lucerne, Switzerland, 2002, pp. 499–506.
[25] A. Esquirol, N.P. Brandon, J.A. Kilner, Solid State Ionics, submitted for publication.
[26] A. Esquirol, N. Brandon, N. Bonanos, J. Kilner, M. Mogensen, B.C.H. Steele, in: J. Huijsmans (Ed.), Proceedings of Fifth European Solid Oxide Fuel Cell Forum, vol. 1, Lucerne, Switzerland, 2002, pp. 225–232.
[27] M. Godickemeier, K. Sasaki, L.J. Gauckler, I. Riess, Solid State Ionics 86–88 (1996) 691–701.
[28] M. Godickemeier, L.J. Gauckler, J. Electrochem. Soc. 145 (2) (1998) 414–421.
[29] M. Sahibzada, R.A. Rudkin, B.C.H. Steele, I.S. Metcalfe, J.A. Kilner, SOFC V, vol. 97-18, Electrochemical Society, USA, 1997, p. 244.
[30] A.H.P. Skelland, Diffusional Mass Transfer, John Wiley & Sons, 1974.